






In Situ X-ray Diffraction Investigation of Hydrogen Effects on Deformation-Induced Phase Transformation in Forged and Additively Manufactured 304L Stainless Steels

SAMANTHA K. LAWRENCE ^{1,5}, REEJU POKHAREL,¹
BJØRN CLAUSEN ¹, DONALD W. BROWN,¹ CHRIS SAN MARCHI ²,
MARY K. O'BRIEN,¹ SANGWON LEE,³ JUN-SANG PARK,⁴
and PETER KENESEI⁴

1.—Los Alamos National Laboratory, PO Box 1663, Los Alamos, NM 87545, USA. 2.—Sandia National Laboratories, 7011 East Ave., Livermore, CA 94550, USA. 3.—University of Michigan, 500 S. State St., Ann Arbor, MI 48109, USA. 4.—Advanced Photon Source, Argonne National Laboratory, 9700 South Cass Avenue, Lemont, IL 60439, USA. 5.—e-mail: slawrence@lanl.gov

This study utilized high energy synchrotron x-ray diffraction to probe microstructural evolution during uniaxial deformation of conventionally manufactured and additively manufactured (AM) 304L stainless steel with and without internal hydrogen. The objective of this effort is to highlight the effect of hydrogen on deformation-induced martensite phase transformations in austenitic stainless steels. Solute hydrogen depresses the required applied strain to initiate austenite transformation to ϵ -martensite and α' -martensite in both forged and AM stainless steel. Similarly, the total fraction of transformation product is larger when the microstructure is saturated with hydrogen. Deformation induced phase transformations also lead to a variation in strain partitioning behavior, which is linked to the chemical composition and stacking fault energy of the starting and hydrogen-charged materials.

INTRODUCTION

Austenitic stainless steels are used extensively in hydrogen-containing environments, including for high-pressure hydrogen gas service, where high toughness, ductility, and strength are advantageous properties. These attributes can be achieved in austenitic stainless steels through twinning induced plasticity (TWIP) or transformation induced plasticity (TRIP) effects. Mechanical behavior of this class of steels depends on the stability of the austenite phase, and therefore the propensity for TRIP behavior, which is further influenced by material microstructure, stacking fault energy (SFE), and deformation conditions.¹ AISI type 304, and its variants, is considered a metastable austenitic stainless steel in reference

to its propensity for deformation-induced phase transformation at room temperature. Deformation-induced transformation results in two distinct phases: hexagonal close packed (HCP) ϵ -martensite and body centered tetragonal (BCT) or body centered cubic (BCC) α' -martensite.^{2–5} The kinetics of the FCC \rightarrow HCP \rightarrow BCC strain-induced transformation path in 304 stainless steel has been described previously.² Olsen and Cohen⁴ proposed that in austenitic Fe-Ni-Cr alloys, a shear-induced FCC to HCP phase transformation could occur simply by the passage of a Shockley partial dislocation on every *second* close packed {111} plane, which changes the ABCABC stacking to ABABAB stacking. The passage of these partials will leave behind stacking faults on every other plane, resulting in a “banded” microstructure, as shown with transmission electron microscopy (TEM).³ The intersections of such shear bands have been shown to be effective nucleation sites for strain-induced α' -martensite formation;^{6,7} similarly, it is possible for α' -

martensite to form at annealing twin boundaries.⁸ It is important to note the structural similarity between ε -martensite formation and austenite deformation twin formation, which belies their common origin, namely glide of extended dislocations. In the case of deformation twins, stacking faults are assembled by successive glide of extended dislocations on *adjacent* {111} planes, which reverses the stacking from ABCABC to CBACBA at the twin plane.

Alloy content is important to the deformation behavior and austenite stability of metastable austenitic stainless steels. Intrinsic stacking fault energy has been used as a metric correlating alloy composition to hydrogen degradation susceptibility.^{9,10} Gibbs et al.¹¹ have shown that austenitic stainless steels with a variety of compositions display higher sensitivity to hydrogen degradation of tensile ductility when the SFE is between 20 mJ m^{-2} and 40 mJ m^{-2} . This regime also corresponds to alloys that have an increasing propensity for planar slip with decreasing SFE, which promotes strain localization on a reduced number of slip planes,¹² exacerbating hydrogen-assisted fracture. Further, typical deformation behavior can be bounded by specific SFE ranges. For example, transformation from γ to ε or α' -martensite typically occurs if SFE is below 20 mJ m^{-2} , whereas mechanical twinning is reported if SFE falls between 15 and 30 mJ m^{-2} .¹³ Both twinning and transformation may be promoted if SFE lies in the relatively small range of $15\text{--}20 \text{ mJ m}^{-2}$.¹⁴

Metal microstructure can also significantly impact performance in hydrogen environments. Several studies have pointed to subtle microstructural variation, such as compositional gradients or the presence of ferrite, as a factor in hydrogen-assisted fracture behavior.^{15,16} Metal additive manufacturing (AM) is an emerging manufacturing technique that enables production of unique component configurations through selective melting and solidification of a feedstock. The microstructures and defect populations produced by AM are distinct from typical wrought products and influence material performance in aggressive environments, including hydrogen service.^{17–21} Similarly, it is important to note that two 304L stainless steels

produced by different processing routes, for example AM versus traditional processing, may have slightly different compositions, which may also influence material performance.

In this study we have deformed non-charged and hydrogen charged forged 304L and AM 304L *in-situ* while collecting synchrotron x-ray diffraction data to probe microstructural evolution, including deformation-induced phase transformations, and strain partitioning behavior. The data highlight unique aspects of hydrogen-deformation interactions, primarily accounted for by differences in stacking fault energy, for two 304L stainless steels produced with distinct processing methods having subtly distinct chemical compositions.

EXPERIMENTAL

The starting materials were 304L stainless steel produced by forging operations or by laser powder bed fusion additive manufacturing; the chemical composition for each material is shown in Table I. The forging was prepared by closed-die extrusion of a 102 mm diameter bar followed by upset forging to a diameter of 83 mm using a high energy rate forging (HERF) technique. For all HERF steps, the forging preforms were preheated to 1116 K prior to forging. All forging and annealing steps were immediately followed by water quenching. Full details of the forging process have been published elsewhere.²²

The additively manufactured material was built using an Electro-Optical Systems (EOS) M280 with build parameters that have been enumerated previously.²³ Briefly, large D-ring components with a tall vertical plate section were fabricated on a 50.5-mm-thick 304L baseplate with a vertical build direction using the EOS-developed PH-1 $20 \mu\text{m}$ (layer height) setting. Aside from layer height ($20 \mu\text{m}$), most of the build parameters were obscured by the proprietary software.

The as-received microstructures for the forged and AM material are depicted in Fig. 1. Samples from each starting material were mechanically polished by standard metallographic procedures then vibratory polished in a $0.2 \mu\text{m}$ colloidal silica suspension for several hours. Electron backscatter diffraction (EBSD) maps were collected with an EDAX Hikari Super EBSD detector using a

Table I. Approximate composition (wt. pct.) of the as-built 304L stainless steel and the as-forged 304L stainless steel

Material Form	Fe	Cr	Ni	Mn	Si	C	N	O	S	P
AM	Bal.	18.4	9.80	1.50	0.53	0.015	0.05	0.019	0.003	0.012
Forging	Bal.	19.64	10.60	1.62	0.65	0.028	0.04	NR1	0.0042	0.020

1: Not Reported (NR)

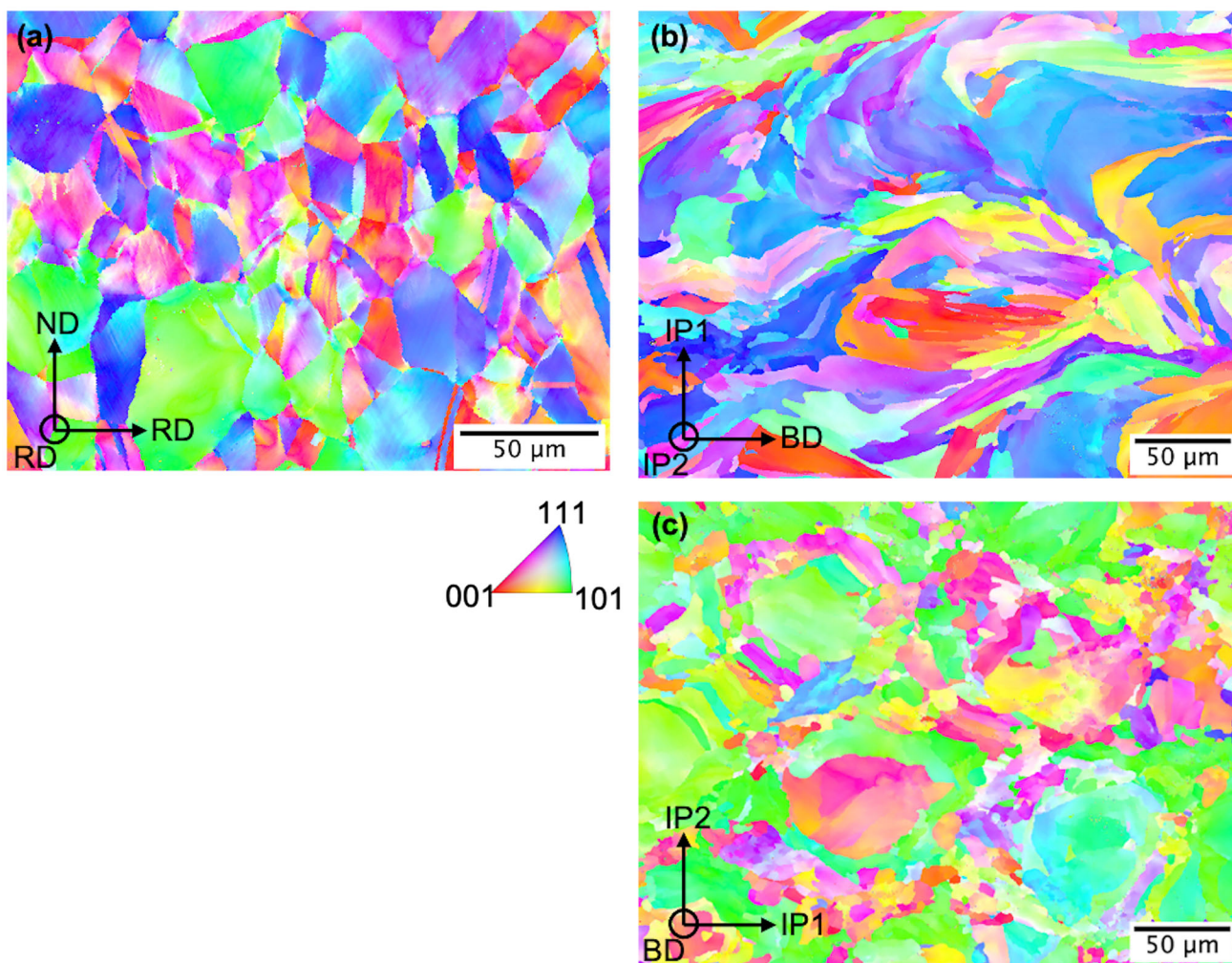


Fig. 1. EBSD inverse pole figure maps for as-received forged 304L stainless steel (a) and as-received AM 304L stainless steel (b, c). In (a) the normal direction, ND, is parallel to the forging direction while the two radial directions, RD, are non-unique. In (b, c) the build direction, BD, is unique, while there are also two non-unique in-plane directions, IP1 and IP2.

ThermoFischer Inspect F scanning electron microscope and an accelerating voltage of 20.0 kV. For the forged sample, a step size of $0.6 \mu\text{m}$ was utilized, while a $0.5 \mu\text{m}$ step size was used for the AM samples. The EBSD data was analyzed using OIM Analysis v8 software.

Specially designed sub-size tensile samples with a square gauge cross section ($1 \text{ mm} \times 1 \text{ mm}$, gauge length 1.5 mm), shown in Fig. 2, were extracted from forged and additively manufactured SS 304L parts via electrical discharge machining. Specimens from the AM material were extracted from the monolithic plate section of the D-ring, with the loading axis perpendicular to the build direction. Similarly, specimens from the forging were extracted with the loading axis perpendicular to the upset forging direction. Atomic hydrogen was dissolved into a subset of specimens by charging in high-pressure hydrogen gas at elevated temperature following a standard procedure enumerated in other works.^{24,25} Specimens were charged at a

hydrogen gas pressure of 138 MPa and a temperature of 573 K for 96 h to achieve a uniform hydrogen concentration of 140 ppm by weight. Hydrogen concentrations were measured with inert gas fusion testing, as described elsewhere.²⁶ Before straining, H-charged specimens which had been stored in an ultralow temperature freezer ($\sim 223 \text{ K}$) were held at room temperature (RT, $\sim 298 \text{ K}$) for 1 h, to allow the sample to equilibrate to ambient temperature. For simplicity, the following nomenclature will be used to identify materials/conditions: NC FG and HC FG refer to non-charged forged and hydrogen-charged forged samples, while NC AM and HC AM refer to non-charged AM and hydrogen-charged AM samples, respectively.

Uniaxial tensile tests were performed at the 1-ID-E endstation at the Advanced Photon Source (APS) at Argonne National Laboratory using a MTS 858 servo-hydraulic load frame with the Rotation and Axial Motion Stage (RAMS) insert, a device specially designed to fit within the load frame to enable

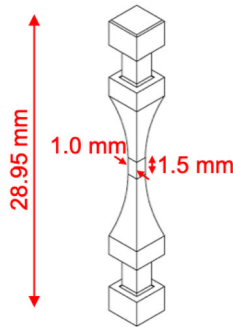


Fig. 2. Specially designed sub-size tensile sample for use with the RAMS insert in the MTS load frame at the 1-ID-E endstation at the APS.

unobstructed sample rotation and deformation during an x-ray experiment.²⁷ The load frame was operated under actuator displacement control at a constant rate of 0.005 mm/s yielding an initial engineering strain rate of $3 \times 10^{-3} \text{ s}^{-1}$ (calculated by dividing the displacement rate by the specimen gage length). Figure 3 presents the true stress–strain curves collected during interrupted tensile testing. Refer to online supplementary material for engineering stress–strain curves.

Monochromatic x-rays with an energy of 71.68 keV were produced by the superconducting undulator²⁸ and 1-ID high-energy monochromator.²⁹ The test specimen cross-section was illuminated by a $1.8 \times 0.1 \text{ mm}^2$ beam, which corresponds to approximately 1000 grains in the illuminated volume. During each diffraction measurement 90 different diffraction patterns were recorded at 2-degree integration angles and 0.9 s exposure times at each load step, with the displacement held constant during the measurements. This led to the observed load drops in the stress–strain response (Fig. 3a and b), which are indicative of stress relaxation of the material during the diffraction measurements, when the specimens were held at a constant displacement. The diffraction data from the 90 projections were then summed to perform phase fraction and strain analysis. Scattered x-rays were collected on a 2-dimensional GE 41RT detector with 2048×2048 pixels ($0.200 \times 0.200 \text{ mm}^2$ pixel size) roughly centered on the straight-through beam and positioned 1004 mm from the sample. As positioned, the detector subtended roughly 10° of 2θ enabling the collection of 6 Debye–Scherrer rings from austenite, 5 α' -martensite rings, and 12 ε -martensite rings.

The specimens were initially installed only in the bottom grip of the RAMS device in order to collect lattice parameter and texture measurements in the unloaded condition (*i.e.* as-machined or as-charged). Specimens were then gripped in both fixtures and pre-loaded to 4.45 N (approximately 5 MPa, with slight variation based on measured cross sectional areas) in tension and initial diffraction patterns were collected. Each specimen was then strained in

predetermined increments, concluding at approximately the ultimate tensile strength (UTS) of the material, as estimated from previous work.^{21,30} Tensile deformation was interrupted at about six points through the elastic regime and eight to ten points through the plastic regime; diffraction patterns were collected while the sample was rotated at each interruption, thereby measuring the evolution of lattice parameter and phase fractions as a function of applied load. Upon reaching the approximate UTS, the test was stopped and the sample slowly unloaded to 5 MPa, whereupon final diffraction patterns were collected.

RESULTS

Deformation-Induced Phase Transformations

The independent and combined effects of processing and solute hydrogen on mechanical properties and phase transformations in forged and AM 304L are shown in Fig. 3. As expected, hydrogen charging increases the 0.2% offset yield stress of both forged and AM SS about 20% (Fig. 3a and b), consistent with results from macroscale tensile testing.²⁵ Notably, the AM samples, even those containing internal hydrogen, sustained strains in excess of 30% without failure.

Evaluating the phase fraction evolution (Fig. 3c and d) for the non-charged samples reveals that the γ -austenitic microstructure (face centered cubic, FCC) of the forged 304L (NC FG) is stable throughout the loading and unloading path imparted, as no ε -epsilon martensite or α' -alpha prime martensite phases are observed to form during deformation in the current tests. In contrast, both ε and α' phases are formed during deformation of the NC AM sample. Note that the ε -martensite phase forms prior to the α' phase, consistent with other reports in literature that ε -martensite is an intermediate product in the $\gamma \rightarrow \alpha'$ transformation.^{6,31–33} In the NC AM sample, the ε -martensite phase is first observed at a macroscopic true strain value, $e = 0.061$, followed by α' at $e = 0.154$. Another key feature of the deformation-induced phase transformation is the plateau observed in the ε -martensite formation at a phase fraction of ~ 0.027 . Conversely, the transformation to α' -martensite continuously increases to a total weight fraction of 0.075. This observation suggests two possible effects at large strains: (1) there are insufficient nucleation sites available for new ε -martensite formation and/or (2) ε -martensite may be consumed by the newly forming α' -martensite embryos.^{34–36}

Turning to the hydrogen charged specimens, it is apparent that this concentration of solute hydrogen has a marked effect on the phase transformation behavior observed for both forged and AM SS. Firstly, it is important to highlight that prior to deformation, no martensite phases are detected in the hydrogen charged samples. That is, the elevated temperature and hydrogen pressure used to

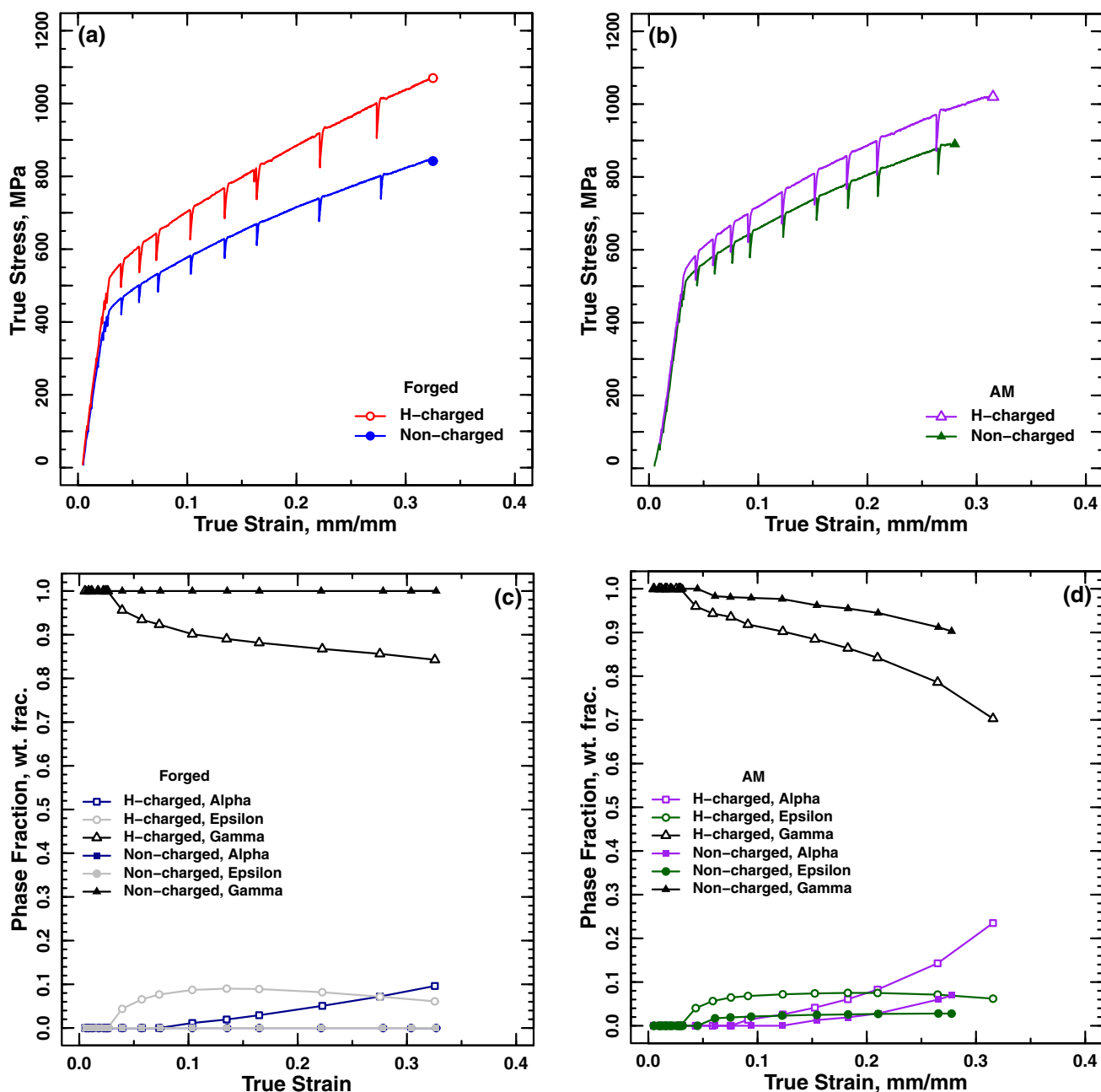


Fig. 3. True stress–strain curves for forged specimens (a) and AM specimens (b) showing locations of load interruptions, indicated by modest load drops, observed during tensile holds for diffraction measurements. Note that the specimens were not pulled to failure, rather the test was stopped after the approximate UTS of each specimen was reached. Phase fraction evolution as a function of true strain for forged specimens (c) and AM specimens (d) both without internal hydrogen and charged with 140 wppm hydrogen.

saturate the microstructure with hydrogen has not inherently promoted martensitic phase transformations. In other words, gas-phase hydrogen charging does not generate sufficient strain to induce phase transformation, unlike cathodic hydrogen charging, which can induce phase transformations in the absence of externally applied stress.^{37–42} This observation is important because it enables some deconvolution of the relative importance of alloy properties and deformation in hydrogen-enhanced phase transformations. First, the HC FG sample

undergoes substantial austenite transformation, where both ϵ -martensite and α' -martensite are observed as strain-induced transformation products. In this case, the onset of the austenite transformation to ϵ -martensite begins at $e = 0.039$; whereas α' -martensite is detected at $e = 0.103$. The ϵ -martensite phase fraction reaches a maximum fraction of about 0.1 at $e = 0.13$, followed by a decrease in the weight fraction to 0.06 when the test ends at $e = 0.32$. In contrast, the weight fraction of α' continuously increases to the end of the test,

Table II. Austenite lattice parameter for each material condition, measured in the unstressed state. Work hardening calculated at 6% engineering strain (see supplementary figure S1 for engineering stress–strain curves), total second phase quantity, and onset strains for ε -martensite and α' -martensite phase transformation in forged and AM 304L for each material condition

Material	Hydrogen content (wppm)	Unstressed γ lattice parameter (Å)	WH @ 6% strain	ε onset true strain (pct.)	α' onset true strain (pct.)	Total second phase (pct)
Forged 304L	0	3.593	3866	N/A	N/A	0
Forged 304L	140	3.595	4424	3.9	10.3	17
AM 304L	0	3.592	4067	6.1	15.4	10.2
AM 304L	140	3.594	5002	4.3	9.1	32.8

reaching a total weight fraction of 0.10. Similar phase fraction evolution behaviors are observed for the HC AM sample. In particular, the austenite transformation to ε -martensite begins at $e = 0.043$, reaches a maximum weight fraction value of 0.075 at $e = 0.18$, and then decreases to a weight fraction of about 0.06 at the end of the test. The α' -martensite transformation begins at $e = 0.091$ and reaches a maximum weight fraction of 0.27 at test end, significantly surpassing the total transformation product observed in the HC FG and NC AM samples. Relevant strain/phase fraction combinations are collected in Table II for ease of interpretation.

Hydrogen Effect on Lattice Parameter and Lattice Strains

Lattice parameters were measured *in-situ* during tensile loading. In the initial (unstressed) conditions, all FG and AM samples were single phase austenite, therefore only the change in the austenite lattice parameter can be determined with respect to a reference, zero-load, value. Initial longitudinal (*i.e.* parallel to the loading direction) lattice parameters for each material condition are collected in Table II. For brevity, transverse lattice parameters are not tabulated, but the trends are consistent with longitudinal values. Comparing the lattice parameter in the NC and HC conditions reveals that 140 wppm internal hydrogen causes a lattice expansion; the longitudinal lattice parameter increases 0.044% and 0.045% for the FG and AM steels, respectively.

The incremental change in lattice parameter throughout tensile straining is used to compute lattice strain, which is a generalized term referring to elastic distortions. Other more precise terms for describing elastic distortion of the lattice are “ hkl -specific strains” and “phase strains”. First, hkl -specific strains are determined from single peak fitting using the following equation:

$$\varepsilon_i^{hkl} = \frac{d_i^{hkl} - d_0^{hkl}}{d_0^{hkl}}, \quad (1)$$

where d_i^{hkl} represents the interplanar spacing along a specific $\{hkl\}$ plane normal aligned with the diffraction vector determined at an applied stress and d_0^{hkl} is the reference d-spacing. Similarly, phase strains are uniquely determined for each phase from the volume averaged lattice parameter determined from Rietveld refinement of the entire diffraction pattern as follows:⁴³

$$\varepsilon_i^{ph} = \frac{\alpha_i^{ph} - \alpha_0^{ph}}{\alpha_0^{ph}}. \quad (2)$$

In Eq. 2 ph refers to the crystallographic phase for which the strain is calculated (austenite in this case), i refers to the sample direction as defined by the diffraction vector, α_i^{ph} is the lattice parameter determined at an applied stress, and α_0^{ph} is the reference lattice parameter. Since both steels are initially single-phase austenite, the reference d-spacing and reference lattice parameter for austenite are taken in the unloaded condition.

Figure 4a and b show the longitudinal austenite hkl -dependent strains for the forged (a) and AM (b) materials. The $\{311\}$, $\{220\}$, and $\{111\}$ orientations of austenite are plotted because they have been shown to have the most linear elastic strain responses.⁴⁴ The variation in orientation dependent strain observed below the elastic limit is caused by the known elastic anisotropy of austenitic steel.^{43,45} After bulk plasticity initiates, grains with $\{220\}$ and $\{111\}$ plane normals parallel to the loading axis display a minimal rate of increase of lattice strain with corresponding macroscopic true stress increments. This “saturation” behavior indicates that these grains are relaxing, by deforming plastically, and fail to carry subsequent increases of macroscopic stress.⁴³ Saturation behavior may indicate that these planes are initially well-oriented for slip. Conversely, the (311) oriented grains accumulate strain throughout the tensile deformation and likely carry the load partitioned from the relaxing (111) and (220) grains. Load transfer among grain orientations is characteristic of the $(111) \langle 110 \rangle$ slip system and the similarity in trends between the

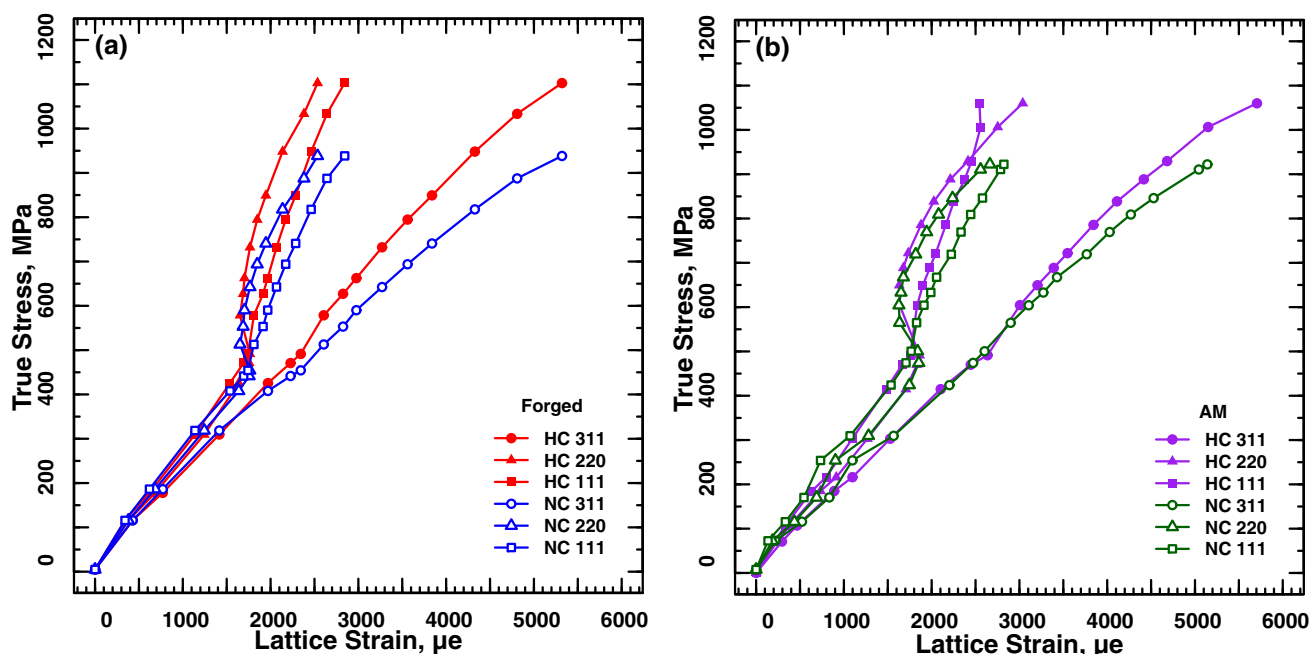


Fig. 4. Austenite *hkl*-specific strains versus macroscopic true stress for the {311}, {220}, and {111} orientations for each specimen condition: forged material (a) and AM material (b).

forged and AM materials may be linked to generally similar initial dislocation densities imparted by the HERF and AM processes used to manufacture the starting materials.

Since lattice strains are a measure of stress on the lattice, a pseudo “stress–strain” curve for the austenite phase in each material condition can be plotted using austenite phase strain in place of the stress axis, as in Fig. 5. Additionally, the evolution of macroscopic true stress as a function of austenite phase strain is plotted in Fig. 6. In both Figs. 5 and 6, a shift away from the linear evolution of phase strain with respect to macroscopic strain or true stress can correspond to changes in stress transfer between phases.⁴⁶ Since only austenite phase strains are shown, deviations from linear can imply transfer of stress from the austenite to a deformation-induced martensite phase and an associated change in deformation mechanism.

The trends of the curves for the NC FG and HC FG samples in Fig. 5a are similar to the composite stress–strain curves in Fig. 3b and the NC and HC curve trajectories do not diverge appreciably from each other. This suggests that the austenite phase in the HC sample continues to support a proportional amount of strain throughout loading, despite the occurrence of deformation induced phase transformations. Similar behavior is observed in Fig. 6, which plots the macroscopic true stress versus longitudinal austenite phase strain for each sample. The slopes of the curves for both NC FG and HC FG samples increase approximately linearly after the onset of yielding, with an offset from the linear elastic portion of the curve caused by anisotropy, confirming that the austenite phase continues to

accumulate strain throughout the tensile test. Considering the AM samples, linear hardening for the NC AM sample is shown in Fig. 5b; in contrast, the austenite phase strain in HC AM sample diverges from the NC AM phase strain (Fig. 5) and the shape of the HC AM phase strain curve is noticeably different from the HC AM composite stress–strain curve (Fig. 3b). The plateau in phase strain of the HC AM after $\epsilon \sim 0.12$ (Fig. 5b) and the associated arrest in austenite phase strain (slope becomes nearly vertical) after a true stress of ~ 660 MPa (Fig. 6) indicates that load is partitioned from the austenite phase to the harder martensite phase in this specific case.

DISCUSSION

The combination of phase fraction and phase strain evolution provide a framework for assessing the influence of material condition on deformation behavior. Of the four alloy/charging conditions tested here, the NC FG will be considered as a baseline condition because no deformation-induced phase transformation is observed in this condition. Beyond the macroscopic 0.2% offset yield stress, plastic deformation of the austenite proceeds, accompanied by some work hardening, as observed in Figs. 3a and 5a. The austenite phase strain increases continuously for every increment of macroscopic stress, as shown in Fig. 6. Several possibilities exist for the lack of a deformation induced phase transformation in the NC FG sample. It is possible that some limited transformation occurred in another portion of the material that is not observed in the area probed by the beam. It is

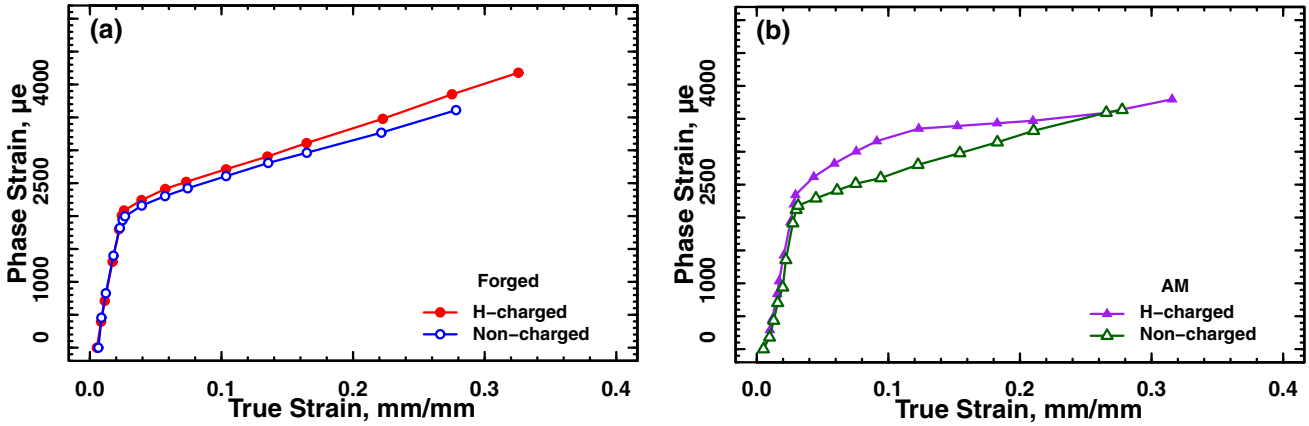


Fig. 5. Austenite phase strains versus macroscopic strain, where phase strains are calculated from measured lattice parameters for each specimen condition: forged material (a) and AM material (b).

possible that no transformation is observed because the test was halted while deformation was still uniform (*i.e.* no necking occurred). Metastable austenite has been shown to be highly sensitive to composition, strain level and strain rate in the vicinity of room temperature,⁴⁷ even resisting martensite transformation until post-uniform deformation for richer compositions. Alternatively, the behavior may be more directly linked with stacking fault energy (SFE), which is suggested to influence the deformation behavior of austenitic steels and is dependent on composition. In general, transformation from γ to ϵ or α' -martensite typically occurs if SFE is below 20 mJ m^{-2} , whereas mechanical twinning is reported if SFE falls between 15 mJ m^{-2} and 30 mJ m^{-2} ,¹³ both twinning and transformation may be promoted if SFE lies between 15 mJ m^{-2} and 20 mJ m^{-2} .¹⁴ Intrinsic SFE (γ_{SFE}) for the non-charged FG and AM material was estimated using the calculation tool developed by Gibbs et al.,¹¹ which is based on the thermodynamic driving force for phase transformation to create a stacking fault ($\Delta G^{\gamma \rightarrow \epsilon}$) within a parent crystal, following the methodology of Olsen and Cohen,^{4,48} as in Eq. 3:

$$\gamma_{SFE} = 2\rho(\Delta G^{\gamma \rightarrow \epsilon}) + 2\sigma \quad (3)$$

Here ρ is the molar surface density of atoms on the $\{111\}^{\gamma}$ crystal planes and σ is the interfacial energy per unit area of the stacking fault. The SFE of a given alloy composition can be estimated if sufficient thermodynamic data are available to calculate the formation energy of the ϵ -martensite phase. Using this formalism, the calculated SFE of the baseline NC FG material is 22.7 mJ m^{-2} . Therefore, the NC FG material falls in a SFE range where mechanical twinning is the most favorable deformation mechanism, as opposed to transformation. The x-ray diffraction data collected in the current study does not provide a measure of twinning propensity. However, favorability of deformation twinning at the calculated SFE is consistent with observations reported by Sabisch et al.,³¹ who

investigated hydrogen effects on deformation bands using interrupted tensile deformation of the same forged SS 304L as in the present work. Their high-resolution scanning transmission electron microscopy (HRSTEM) and nanobeam diffraction studies illuminate the deformation mechanisms that promote the phase transformation behavior observed in the present work. Specifically, in their study, deformation of non-charged samples up to 20% strain resulted in initial dislocation networks organizing into planar deformation bands composed of austenite deformation twins, eventually intersecting, with only a very small amount of α' -martensite isolated at grain boundaries. Together the x-ray diffraction data collected in the current study and HRSTEM data suggest that the SFE of the NC FG sample is sufficiently high to minimize austenite transformation during deformation.

A clear shift in deformation behavior is observed for the NC AM material. In contrast with the NC FG sample, the initially fully austenitic NC AM sample readily transforms to ϵ -martensite after yielding followed by α' -martensite formation. Considering the macroscopic, composite stress-strain behavior (Fig. 3), the 0.2% offset yield strength of this sample is slightly higher than its NC FG counterpart (true stress values of 512 MPa versus 455 MPa, respectively). This difference is likely linked to variation in chemical composition (Table I) and microstructure (Fig. 1), including dislocation structures.⁴³ After yielding, plastic deformation accompanied by some work hardening is observed (Figs. 3 and 5b). During initial plastic deformation, before any austenite transformation occurs, the austenite phase strains for the NC AM and NC FG samples are parallel and overlaid (Fig. 6). That is, for an increment of macroscopic stress, the phase strains in the two samples are about the same, indicating that the austenite in the NC AM is accommodating deformation in the same manner as the NC FG sample. However, after the onset of α' formation, at a true stress of $\sim 659 \text{ MPa}$ in the NC AM condition,

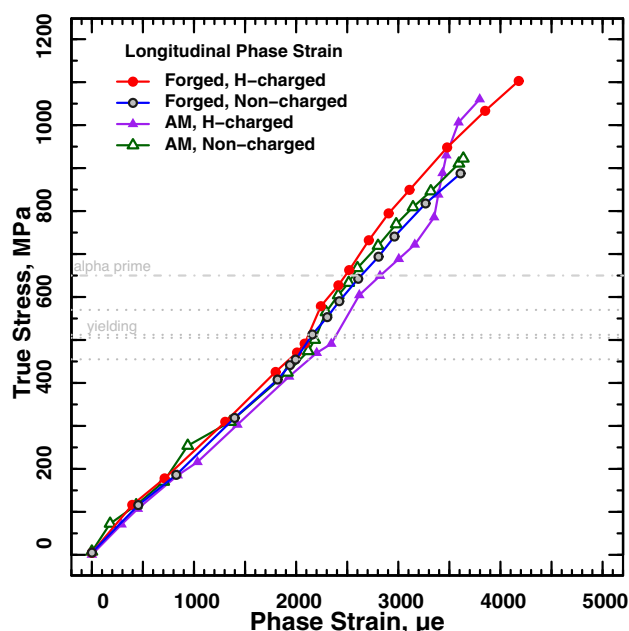


Fig. 6. Longitudinal elastic phase strains in the austenite plotted against true macroscopic stress for each material condition. The dashed lines indicate the yield strength for each sample, in increasing order NC FG, HC FG, NC AM, HC AM. The dot-dash line indicates the approximate onset stress for α' transformation.

the austenite phase strain in the NC AM sample diverges from the NC FG sample. In this regime, for every increment of macroscopic stress, the NC AM austenite phase strain is lower than the NC FG phase strain. This suggests some load partitioning from the austenite to the second phase martensite while the austenite is still plastically deforming; continued strain accumulation in the austenite is consistent with the relatively small fraction of martensite in the structure.

We can also consider the deformation and transformation behaviors in the context of stacking fault energy. The estimated SFE of the NC AM (19.8 mJ m^{-2}) essentially lies on the 20 mJ m^{-2} boundary below which martensite transformation could become the preferred deformation mechanism over twinning.¹³ And, in fact, austenite does transform to martensite in the NC AM sample, but only after measurable plasticity, as highlighted by comparing the onset strain in Fig. 3d with the macroscopic stress-strain curve in Fig. 3b. At the same time, the γ phase continues to accumulate strain throughout tensile loading, as highlighted by the effective hardening behavior shown in Fig. 5b and the increasingly tensile slope after the onset of α' formation in Fig. 6, which may be expected when austenite remains the dominant deforming phase. The sensitivity of SFE to composition,^{49–51} for example the content of Ni, which is an austenite stabilizer, may contribute to the observed difference in transformation behavior between the NC AM and NC FG materials studied here. For the alloys used in this work, the Ni content in the NC AM is 9.8%

and has a SFE of 19.8 mJ m^{-2} as opposed the NC FG with a Ni content of 10.6% and SFE of 22.7 mJ m^{-2} . The NC AM sample experiences strain-induced transformation, while no austenite transformation is detected in the NC FG sample. This result is consistent with an example provided by Galindo-Nava et al.,¹³ who note that increasing the Ni content to 10.5% from the baseline 8% in a 304 SS, increased the estimated SFE to 22 mJ m^{-2} from 17.8 mJ m^{-2} and concomitantly promoted twinning, at the expense of transformation.

Pre-charging both forged and AM material with 140 wppm H has a pronounced effect on the subsequent deformation behavior. Considering the HC FG sample, the macroscopic yield stress increased $\sim 20\%$ from the NC condition as a result of strengthening by the high concentration of hydrogen in solution, consistent with other published results.²⁵ Similarly, a moderate increase in work hardening is observed after yielding (Fig. 3, Table II). After the onset of austenite transformation, the HC FG sample begins to behave similarly to the NC AM material. Specifically, once the α' transformation is activated at true stress of $\sim 660 \text{ MPa}$, the austenite elastic phase strain in the HC FG sample diverges from the slope of the NC curve. In this regime, for every increment of stress, the HC FG austenite phase strain is lower than the NC FG austenite phase strain suggesting that a greater fraction of the load may be transferred to the second phase martensite, although the austenite is still plastically deforming. The magnitude of load partitioning observed in Fig. 6 is greater for the HC FG compared with the NC AM, concomitant with the larger α' and total second phase fraction.

The influence of hydrogen on promotion of deformation-induced phase transformation in the forged 304L is notable and consistent with a similar study using a stable austenitic stainless steel (21Cr-6Ni-9Mn), which reported ε -martensite transformation only after hydrogen charging,⁵² and complementary work with the forged 304L used here, which reported considerably more austenite transformation in the HC condition and minor transformation in the NC condition.³¹ The HRSTEM data presented by Sabisch et al.³¹ again illuminate the connection between deformation and phase transformation behavior for the HC FG material. They observe dislocation networks with extended stacking faults in the unstressed HC (140 wppm) condition. Upon deformation of the hydrogen charged sample up to 20% strain, deformation bands composed of austenite deformation twins and ε -martensite laths form and eventually intersect, with larger quantities of α' -martensite found predominantly at deformation band intersections. It is important to note that shear bands are initially parallel to one another, with few intersections and concomitantly few nucleation sites for α' embryos. As deformation proceeds and secondary slip systems begin to operate, shear

bands will begin to intersect, providing α' -martensite nucleation sites. The deformation (and time) required to develop the necessary nucleation sites likely contributes to the delayed onset of α' -martensite formation observed in the present work.

It is widely suggested that hydrogen lowers the stacking fault energy of austenitic stainless steels and SFE has been considered as a metric for hydrogen performance.^{9,10,38} The mechanisms by which SFE reduction could occur are beyond the scope of the current work. Here we will simply consider that hydrogen interaction with dislocations, stacking faults, or twins may serve to produce an effect that can be captured as an effective reduction in stacking fault energy. Several literature studies attempt to quantify the magnitude of the hydrogen effect on SFE. Zhou et al.⁵³ calculate stacking fault energies by performing time averaged molecular dynamics simulations using a Fe-Ni-Cr-H quaternary interatomic potential and report SFE reduction ranging between 8.5% and 100% depending on hydrogen concentration at a dislocation core. Pontini et al.⁵⁴ measured stacking fault energy reduction via XRD with the aid of TEM and report a hydrogen-induced SFE reduction for AISI 304 stainless steel at room temperature of 37%, roughly in the middle of the range reported by Zhou et al. Here, we apply the reduction reported by Pontini to the baseline SFE for the forged material and estimate a potential SFE for the HC FG material of 17.3 mJ m^{-2} . At this lower SFE value both twinning and martensite transformation are likely promoted, consistent with x-ray diffraction measurement of martensite fraction in the present work and with HRSTEM imaging of twins and martensite laths by Sabisch et al.³¹ Essentially, internal hydrogen enables HC FG material to behave like NC AM, which has a lower initial SFE due to chemical composition differences, and promotes austenite deformation.

The HC AM material displays the most complicated deformation behavior. Beyond the elastic limit, the work hardening in this material is higher than for all other samples (Fig. 3, Table II). Additionally, the austenite transformation to ε -martensite occurs almost immediately upon yielding; the elastic limit is $\sim 571 \text{ MPa}$, with ε -martensite formation at $\sim 578 \text{ MPa}$ (Fig. 6). In this early stage of plastic deformation, twinning may be discouraged in favor of ε -martensite formation, though dislocation-dislocation interactions continue. After the onset of α' transformation, the hardening behavior indicated in Fig. 5b plateaus and the fraction of α' begins to increase parabolically (Fig. 3d). In this regime there may be sufficient intersecting ε bands that serve as viable α' nucleation sites. Similarly, after the α' transformation begins at $\sim 659 \text{ MPa}$, the slope of the HC AM curve in Fig. 6 becomes nearly vertical, which indicates saturation in the austenite phase strain. That is, the elastic phase strain ceases to increase with each increment of

stress. Here, deformation is accommodated in the composite material by partitioning load from the austenite to the second phase martensite. In this regime it is possible that each increase in stress activates a transformation and that austenite hardening opportunities are diverted by transformation even if plasticity mechanisms are still active. This behavior is similar to behavior observed in some TRIP steels.^{55,56} We again hypothesize that hydrogen influences the material in a way that can be described by estimating a SFE reduction. Applying the SFE reduction calculated by Pontini,⁵⁴ we estimate a SFE with hydrogen of 15.1 mJ m^{-2} for the HC AM material. The current phase transformation results are consistent with deformation regime maps in Ref. 13, which predict both ε and α' -martensite transformation will be promoted at this low SFE, with a potential preference towards α' -martensite formation. In fact, the diffraction results indicate that a much larger fraction of α' -martensite is formed in the HC AM at large strains, as compared with the other conditions.

CONCLUSION

In situ x-ray diffraction measurements were completed during deformation of forged and AM 304L stainless steel in non-charged and hydrogen charged conditions. The key findings are as follows:

1. Deformation induced phase transformations ($\gamma \rightarrow \varepsilon/\alpha'$) only occurred after hydrogen charging the forged 304L, whereas deformation induced phase transformations occurred in both the non-charged and hydrogen-charged AM 304L stainless steel.
2. Hydrogen charging with 140 wppm H depresses the required applied strain to initiate austenite transformation to ε martensite and subsequent α' martensite formation.
3. Hydrogen charging with 140 wppm H increases the work hardening rate and yield strength of the material without an associated reduction in ductility.
4. In the hydrogen-charged samples, the weight fraction of ε -martensite decreases after reaching a maximum value on the order of 0.08, while α' -martensite continued to form, suggesting that the transformation to ε -martensite becomes unfavorable and ε -martensite may be consumed by the α' -martensite growth.
5. The total martensite fraction in the hydrogen-charged AM 304L was considerably larger than for either the NC AM or HC FG material.
6. Strain partitioning from austenite to martensite occurs at large strains for the hydrogen-charged AM 304L, whereas the austenite phase in the non-charged AM and both forged samples accumulates significant plastic strain throughout the test duration with minimal, if any, load partitioning.

Austenite transformation behavior is linked to the calculated stacking fault energy of the AM and forged materials, which vary slightly in composition. Further, hydrogen is proposed to influence stacking fault formation, which subsequently affects martensite formation during deformation.

SUPPLEMENTARY INFORMATION

The online version contains supplementary material available at <https://doi.org/10.1007/s11837-023-05787-6>.

ACKNOWLEDGEMENTS

The authors wish to thank Dr. Paul J. Gibbs of LANL for thought-provoking discussion related to hydrogen-materials interactions and lattice strain data, as well as Dr. Alexandra G. Glover and Dr. Virginia K. Euser of LANL for critical review of the manuscript and discussion of strain partitioning and austenite transformation kinetics. RP, BC, DWB, and SL acknowledge support from the Dynamic Materials Properties Campaign under the U.S. Department of Energy National Nuclear Security Administration. This research used resources of the Advanced Photon Source, a U.S. Department of Energy (DOE) Office of Science User Facility operated for the DOE Office of Science by Argonne National Laboratory under Contract No. DE-AC02-06CH11357. This work was supported by the U.S. Department of Energy through Los Alamos National Laboratory and Sandia National Laboratories. Los Alamos National Laboratory is operated by Triad National Security, LLC, for the National Nuclear Security Administration of U.S. Department of Energy (Contract No. 89233218CNA000001). Sandia National Laboratories is a multi-mission laboratory managed and operated by National Technology and Engineering Solutions of Sandia, LLC., a wholly owned subsidiary of Honeywell International, Inc., for the U.S. Department of Energy's National Nuclear Security Administration (NNSA) under contract DE-NA-0003525.

CONFLICT OF INTEREST

On behalf of all authors, the corresponding author states that there is no conflict of interest.

REFERENCES

1. S. Allain, J.-P. Chateau, O. Bouaziz, S. Migot and N. Guelton, *Mater. Sci. Eng. A* 387–389, 158 (2004).
2. G.B. Olson and M. Cohen, *Metall. Trans. A* 6, 791 (1975).
3. G.B. Olson and M. Cohen, *Metall. Trans. A* 7A, 1897 (1976).
4. G.B. Olson and M. Cohen, *Metall. Trans. A* 7A, 1905 (1976).
5. G.B. Olson and M. Cohen, *Metall. Trans. A* 7A, 1915 (1976).

6. J.A. Venables, *Philos. Mag. J. Theor. Exp. Appl. Phys.* 7, 35 (1962).
7. F. Lacroisey and A. Pineau, *Metall. Mater. Trans. B* 3, 391 (1972).
8. G.R. Caskey Jr, *Environmental Degradation of Engineering Materials in Hydrogen* ed. M.R. Louthan, R.P. McNitt and R.D. Sisson (Virginia Polytechnic Institute, Blacksburg, 1981), p. 283.
9. B.C. Odegard, J.A. Brooks and A.J. West, *Effects of Hydrogen. Behaviour Materials*, ed. A.W. Thomson and I.M. Bernstein (The Metallurgical Society of AIME, Moran, WY, 1976), p. 116.
10. G.R. Jr Caskey, *Hydrogen Compatibility Handbook for Stainless Steels* (Aikin, Savannah River Lab, 1983), p156.
11. P.J. Gibbs, P.D. Hough, K. Thürmer, B.P. Somerday, C. San Marchi and J.A. Zimmerman, *JOM* 72, 1982 (2020).
12. H.K. Birnbaum and P. Sofronis, *Mater. Sci. Eng. A* 176, 191 (1994).
13. E.I. Galindo-Nava and P.E.J. Rivera-Díaz-del-Castillo, *Acta Mater.* 128, 120 (2017).
14. Y.F. Shen, X.X. Li, X. Sun, Y.D. Wang and L. Zuo, *Mater. Sci. Eng. A* 552, 514 (2012).
15. B.P. Somerday, M. Dadfarnia, D.K. Balch, K.A. Nibur, C.H. Cadden and P. Sofronis, *Metall. Mater. Trans. A* 40, 2350 (2009).
16. T. Michler, Y. Lee, R.P. Gangloff and J. Naumann, *Int. J. Hydrog. Energy* 34, 3201 (2009).
17. S.-W. Baek, E.J. Song, J.H. Kim, M. Jung, U.B. Baek and S.H. Nahm, *Scr. Mater.* 130, 87 (2017).
18. J.R. Trelewicz, G.P. Halada, O.K. Donaldson and G. Manogharan, *JOM* 68, 850 (2016).
19. J.A. Stull, M.A. Hill, T.J. Lienert, J. Tokash, K. Bohn and D.E. Hooks, *JOM* 70, 2677 (2018).
20. C. San Marchi, J. D. Sugar and D. K. Balch, in *Proc. 3rd Int. Conf. Met. Hydrog.* (Ghent, Belgium, 2018), p. 7.
21. C. San Marchi, T. R. Smith, J. D. Sugar and D. K. Balch, in *Struct. Integr. Addit. Manuf. Parts* (ASTM International, West Conshohocken, PA, 2020), pp. 381–398.
22. H. Jackson, C. San Marchi, D. Balch, B. Somerday and J. Michael, *Metall. Mater. Trans. A* 47, 4334 (2016).
23. G. T. Gray, V. Livescu, P. A. Rigg, C. P. Trujillo, C. M. Cady, S.-R. Chen, J. S. Carpenter, T. J. Lienert, S. J. Fensin, C. M. Knapp, R. A. Beal, B. Morrow, O. F. Dippe, D. R. Jones, D. T. Martinez, J. A. Valdez, *Los Alamos National Laboratory Technical Report* (LANL, Los Alamos, 2016), p. 23/Gray Iii, G., Livescu, V., Rigg, P., Trujillo.
24. S.K. Lawrence, B.P. Somerday and R.A. Karnesky, *JOM* 69, 45 (2017).
25. C. San Marchi, D.K. Balch, K. Nibur and B.P. Somerday, *J. Press. Vessel Technol.* 130, 041401 (2008).
26. S.K. Lawrence, B.P. Somerday, N.R. Moody and D.F. Bahr, *JOM* 66, 1383 (2014).
27. P.A. Shade, B. Blank, J.C. Schuren, T.J. Turner, P. Kenesei, K. Goetze, R.M. Suter, J.V. Bernier, S.F. Li, J. Lind, U. Leinert and J. Almer, *Rev. Sci. Instrum.* 86, 093902 (2015).
28. Y. Ivanyushenkov, K. Harkay, M. Borland, R. Dejus, J. Dooling, C. Doose, L. Emery, J. Fuerst, J. Gagliano, Q. Hasse, M. Kasa, P. Kenesei, V. Sajaev, K. Schroeder, N. Sereno, S. Shastri, Y. Shiroyanagi, D. Skiadopoulos, M. Smith, X. Sun, E. Trakhtenberg, A. Xiao, A. Zholents and E. Gluskin, *Phys. Rev. Accel. Beams* 20, 100701 (2017).
29. S.D. Shastri, K. Fezzaa, A. Mashayekhi, W.-K. Lee, P.B. Fernandez and P.L. Lee, *J. Synchrotron Radiat.* 9, 317 (2002).
30. C. San Marchi, J.A. Ronevich, J.E.C. Sabisch, J.D. Sugar, D.L. Medlin and B.P. Somerday, *Int. J. Hydrog. Energy* 46, 12338 (2021).
31. J.E.C. Sabisch, J.D. Sugar, J. Ronevich, C. San Marchi and D.L. Medlin, *Metall. Mater. Trans. A* 52, 1516 (2021).
32. M. Hatano, Y. Kubota, T. Shobu and S. Mori, *Philos. Mag. Lett.* 96, 220 (2016).
33. G.B. Olson and M. Cohen, *J. Common Met.* 28, 107 (1972).
34. K. Tao, D.W. Brown, S.C. Vogel and H. Choo, *Metall. Mater. Trans. A* 37, 3469 (2006).

35. E. Cakmak, H. Choo, J.-Y. Kang and Y. Ren, *Metall. Mater. Trans. A* 46, 1860 (2015).
36. K. Tao, J.J. Wall, H. Li, D.W. Brown, S.C. Vogel and H. Choo, *J. Appl. Phys.* 100, 123515 (2006).
37. A.P. Bentley and G.C. Smith, *Metall. Trans. A* 17, 1593 (1986).
38. M.L. Holzworth and M.R. Louthan Jr., *Corrosion* 24, 110 (1968).
39. C. Pan, W.Y. Chu, Z.B. Li, D.T. Liang, Y.J. Su, K.W. Gao and L.J. Qiao, *Mater. Sci. Eng. A* 351, 293 (2003).
40. S. Tähtinen, P. Nenonen and H. Hanninen, *Scr. Metall.* 20, 153 (1986).
41. S.M. Teus, V.N. Shyvanyuk and V.G. Gavriljuk, *Mater. Sci. Eng. A* 497, 290 (2008).
42. V. Shivanyuk, *Scr. Mater.* 49, 601 (2003).
43. D.W. Brown, D.P. Adams, L. Balogh, J.S. Carpenter, B. Clausen, G. King, B. Reedlunn, T.A. Palmer, M.C. Maguire and S.C. Vogel, *Metall. Mater. Trans. A* 48, 6055 (2017).
44. B. Clausen, T. Lorentzen and T. Leffers, *Acta Mater.* 46, 3087 (1998).
45. B. Clausen, T. Lorentzen, M.A.M. Bourke and M.R. Daymond, *Mater. Sci. Eng. A* 259, 17 (1999).
46. P.J. Jacques, Q. Furnemont, S. Godet, T. Pardoën, K.T. Conlon and F. Delannay, *Philos. Mag.* 86, 2371 (2006).
47. S.S. Hecker, M.G. Stout, K.P. Staudhammer and J.L. Smith, *Metall. Trans. A* 13, 619 (1982).
48. P.H. Adler, G.B. Olson and W.S. Owen, *Metall. Trans. A* 17, 1725 (1986).
49. G.R. Lehnhoff, K.O. Findley and B.C. De Cooman, *Scr. Mater.* 92, 19 (2014).
50. R.E. Schramm and R.P. Reed, *Metall. Trans. A* 6, 1345 (1975).
51. L. Vitos, J.-O. Nilsson and B. Johansson, *Acta Mater.* 54, 3821 (2006).
52. C. S. Marchi, B. P. Somerday and H. F. Jackson, in *Proc. 2nd International Conf. of Engineering Against Fracture* (Mykonos, Greece, 2011).
53. X.W. Zhou, C. Nowak, R.S. Skelton, M.E. Foster, J.A. Ronevich, C. San Marchi and R.B. Sills, *Int. J. Hydrog. Energy* 47, 651 (2022).
54. A.E. Pontini and J.D. Hermida, *Scr. Mater.* 37, 1831 (1997).
55. P.J. Gibbs, B.C. De Cooman, D.W. Brown, B. Clausen, J.G. Schroth, M.J. Merwin and D.K. Matlock, *Mater. Sci. Eng. A* 609, 323 (2014).
56. S. Cheng, X.-L. Wang, Z. Feng, B. Clausen, H. Choo and P.K. Liaw, *Metall. Mater. Trans. A* 39, 3105 (2008).

Publisher's Note Springer Nature remains neutral with regard to jurisdictional claims in published maps and institutional affiliations.